Proton Density Fat Fraction of Breast Adipose Tissue: Comparison of the Effect of Fat Spectra and Initial Evaluation as a Biomarker

Isobel Gordon[1,2](✉), George Ralli[2], Carolina Fernandes[2], Amy Herlihy[2], and Sir Michael Brady[2,3]

[1] Nuffield Department of Women's and Reproductive Health, University of Oxford, Oxford, England
isobel.gordon@new.ox.ac.uk
[2] Perspectum Ltd., Oxford, England
[3] Department of Oncology, University of Oxford, Oxford, England

Abstract. The composition of breast adipose tissue has been shown to vary according to disease state. Proton density fat fraction (PDFF) is a quantitative MR biomarker which has not yet been thoroughly examined in the characterisation of breast fat; this work therefore explores the estimation of breast-specific PDFF. An MR spectrum derived from healthy breast fat is shown to perform significantly better in PDFF calculation of breast adipose tissue amongst a healthy cohort than either 6-peak or 9-peak subcutaneous fat spectra. Calculated PDFF values of breast adipose tissue suggest a similar composition between healthy breast fat and gluteal fat and a reference value of 91.6 ± 3.0% PDFF is found for healthy breast adipose tissue. Early results indicate that localised regions of lowered adipose PDFF are visible in proximity to both invasive and non-invasive breast cancer; this may be indicative of the inflammation and browning of mammary fat around tumour cells.

Keywords: Breast cancer · Proton density fat fraction · MRI

1 Introduction

Breast cancer is the single most common cancer in the UK [1] and the worldwide leading cause of cancer death amongst women [24]. Early detection of breast cancer greatly improves prognosis; this has led to nationwide screening of asymptomatic women. These screening initiatives exclusively use mammography and are restricted to postmenopausal women typically above the age of 50. The effectiveness of mammography is dramatically reduced in radiologically 'dense'

Supported by the Royal Commission for the Exhibition of 1851 and Perspectum Ltd. We also gratefully acknowledge the provision of MR spectral data by Gene Kim and Pippa Storey at New York University Grossman School of Medicine.

G. Yang et al. (Eds.): MIUA 2022, LNCS 13413, pp. 28–45, 2022.
https://doi.org/10.1007/978-3-031-12053-4_3

breasts [16], which have a high proportion of fibrous, functional tissue compared to fatty tissue. Breast density has been found to be the single most important risk factor for breast cancer in postmenopausal women [6] and thus the reporting of breast density is mandatory in most US states and several other territories.

High-risk younger women and postmenopausal women with dense breasts are increasingly offered 'abbreviated' MRI with protocols which include dynamic contrast enhanced MRI (DCE-MRI). DCE-MRI is primarily used to aid visualisation of increased localised vascularity that may indicate the presence of a tumour. This scan requires the injection of a contrast agent which is poorly tolerated by many patients and has a wide array of side effects. DCE-MRI also takes a substantial proportion of the MR imaging time, even in 'abbreviated' protocols, and is at best semi-quantitative. Current breast MRI protocols focus on detecting localised potential tumour regions despite increasing evidence showing that the composition of the breast parenchyma is important for assessing both pathology and cancer risk [6,28]. Quantitative characterisation of the whole breast parenchyma, rather than only the tumour, could enable the health of the whole breast to be examined and thereby lead to improved estimation of risk and improved patient care.

Proton density fat fraction (PDFF) is a quantitative MR biomarker which has been used extensively in the diagnosis, staging, and monitoring of non-alcoholic fatty liver disease (NAFLD) [22] and non-alcoholic steatohepatitis (NASH) [8]. Henze Bancroft et al. [4] recently demonstrated the use of proton density water fraction (PDWF) as a biomarker of mammographic breast density. However, PDFF has not yet been thoroughly studied as a useful metric in breast tissue characterisation itself. Initial work in this area is promising; a recent study by Hisanaga et al. [13] found that the fat fraction of adipose tissue around invasive breast cancer was associated with lymph node metastasis.

PDFF is typically quantified from multi-echo chemical shift encoded (CSE) MRI acquisitions, which exploit the different precession frequencies of fat and water to estimate fat content. These acquisitions are typically short and entirely non-invasive. Analysis of CSE-MRI acquisitions has typically used both the magnitude and phase information of the MRI signal to determine PDFF. However, such complex information may not be readily available in the clinical setting, and the inclusion of complex data can introduce artefacts which may impact PDFF quantification. Triay Bagur et al. [3] recently introduced a magnitude-only method (MAGO) to estimate liver PDFF which has been demonstrated to be robust to imaging artefacts.

To date, the incorporation of a breast-specific fat spectrum into PDFF calculation has not been studied. For example, Henze Bancroft et al. [4] assumed breast fat and subcutaneous fat to be equivalent, whilst the IDEAL-IQ fat fraction maps used in Hisanaga et al. [13] employ a liver-specific fat spectrum.

Human adipose tissue may generally be classified into two subtypes: brown adipose tissue (BAT), which is primarily used for heat generation, and white adipose tissue (WAT) which is predominantly used for energy storage. The PDFF of white and brown adipose tissue has been approximated through determination of PDFF in supraclavicular and gluteal adipose tissue [9]. BAT was found to have significantly lower PDFF than WAT; this is reflective of the lower lipid content and higher intracellular water content of BAT.

White adipocytes may differentiate into brown-like ('beige') adipocytes in a process referred to as 'browning'. Importantly, breast cancer tumour growth has been associated with the browning of mammary fat close to the tumour [23,26]. Moreover, Bos et al. [5] found larger volumes of BAT throughout the body in patients with cancer whilst Cao et al. [7] found three times as much BAT in breast cancer patients compared to patients with other cancers.

Furthermore, the release of proinflammatory cytokines has been associated with decreased lipid content in cancer-adjacent adipose tissue [18] and inflammation of adipose tissue has been found to be associated with both ductal carcinoma in situ [2] and invasive breast cancer [25]. Moreover, perilesional oedema may be found in proximity to invasive breast cancer; this may correlate to the aggressiveness of the disease [19].

We hypothesise that lower PDFF in breast adipose tissue may be associated with the browning and inflammation of mammary fat, or with perilesional oedema, and thereby associated with tumour growth. This may either be localised, further aiding the detection and categorisation of tumours, or spread through the breast, improving assessment of breast cancer risk.

This work explores the estimation of breast-specific PDFF. Firstly, adipose tissue is segmented within the highly heterogeneous breast structure. Next, the performance of five different fat spectra in the calculation of breast adipose PDFF is examined and values are reported across a healthy cohort. Finally, PDFF is examined in the adipose tissue immediately surrounding both cysts and cancerous lesions.

2 Methods

2.1 Data Acquisition

Participants were imaged in the prone position on a Siemens Magnetom Aera 1.5T scanner (Siemens Healthineers AG, Erlangen, Germany) using a bilateral 18-channel breast coil (Siemens Healthineers AG, Erlangen, Germany). Participants were scanned with a 3D axial 6-echo (TE1 = 1.81 ms, delta TE = 1.95 ms) gradient echo protocol designed to minimize T1 bias with a small flip angle (5°). The following additional acquisition parameters were used: TR = 15.0 ms, reconstructed in-plane resolution $1.7 \times 1.7\,\text{mm}^2$, slice thickness 2.0 mm, acquired matrix size 128×128, FOV $440 \times 399\,\text{mm}^2$, bandwidth 1560 Hz/Px. Typically, 80 slices covered the whole of both breasts, though this number was adjusted to ensure full coverage of larger breasts. For a scan with 80 slices, the acquisition time was 2 min and 19 s. Nine participants were additionally scanned with a multi-slice 2D axial 6-echo gradient echo sequence. The parameters were: TE1 = 1.30 ms, delta TE = 2.00 ms, TR = 14.0 ms, flip angle 5°, reconstructed in-plane resolution $1.7 \times 1.7\,\text{mm}^2$, slice thickness 10.0 mm, slice distance factor 50%, acquired matrix size 128×128, FOV $440 \times 399\,\text{mm}^2$, bandwidth 1560 Hz/Px, acquisition time 8 s. Five slices were acquired in the breasts with the position of the central slice matching that of the 3D CSE sequence described above. This sequence, referred to as 'LMS IDEAL' in Triay Bagur et al. [3], has been used extensively for quantification of PDFF in the liver and was acquired for comparative purposes; note that full coverage of the breast is not obtained with this 2D acquisition. In addition to these two gradient echo sequences, a high resolution T1-weighted volumetric scan was obtained for purposes of localisation and anatomical identification.

Forty-six female volunteers were scanned for this study; ethical approval was granted by South Central Ethics (NHS REC 20/WS/0110). Forty-two participants were healthy with no known breast lesions, whilst two volunteers had known breast cysts but were otherwise healthy. The healthy cohort was defined as these forty-four women. In addition, one participant had confirmed ductal carcinoma in situ (DCIS) in the left breast and one participant had confirmed invasive ductal carcinoma (IDC) in the right breast. Both participants with confirmed cancer underwent biopsy on a date at least 4 weeks prior to the MRI scan. The mean age of participants was 41 years (range 24–78 years). Written informed consent was obtained from all subjects prior to scanning.

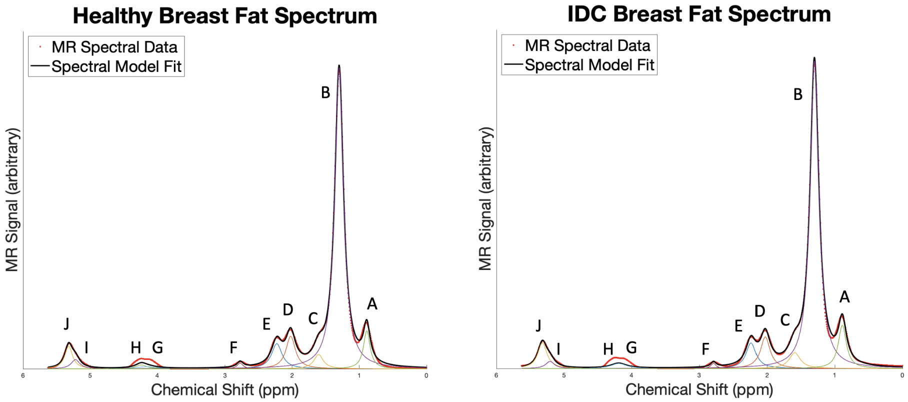

Fig. 1. MR spectra of a participant with no suspicious findings in MR images (designated 'healthy') (left) and a participant with invasive ductal carcinoma (IDC) (right).

2.2 Spectroscopic Analysis

Breast adipose MR spectroscopic data was derived from Freed et al. [10]. The group acquired a three-dimensional sagittal 144-echo gradient-echo sequence with a low flip angle and a bandwidth 694 Hz. A Fourier transform was applied to each voxel with corrections for phase and eddy currents to produce an MR spectrum. A region of interest (ROI) was drawn in the breast adipose tissue; the final spectrum for each patient was found by averaging across all voxels in the

ROI. As Freed et al.'s work concentrated on determining the relative amplitudes of just five select peaks in breast fat, we re-analysed the spectra to determine the relative amplitude of all peaks. We analysed two MR spectra provided by Freed et al.: one from the breast adipose tissue of a woman with no suspicious findings in MR images (designated 'healthy') and one from the breast adipose tissue of a woman with known invasive ductal carcinoma (IDC) (Fig. 1).

To minimize differences in linewidth, the free induction decay (FID) of the spectra were first multiplied by an exponential filter so that the methylene ('B') peak in both spectra had the same linewidth. A spectral model was fitted to the data consisting of a linear baseline and 10 Lorentizian line profiles, each of which corresponded to one of the 10 fat peaks identified by Freed et al. The data was fitted to this model using a non-linear least squares approach. The positions of the Lorentzian peaks were initially set to literature values but allowed to vary during the fit. The R^2 of the final fit to the spectral data was 0.997 in the spectrum taken from the participant with IDC, and 0.998 in the spectrum taken from the healthy participant. Finally, the area under each peak was found through integrating the Lorentzian equation associated with each peak across the whole spectrum (Table 1).

Table 1. Chemical shift values and relative areas of the fitted fat peaks in the MR spectra of the breast adipose tissue of a participant with no suspicious findings in MR images (designated 'healthy') and a participant with invasive ductal carcinoma (IDC).

	Healthy		IDC	
Peak label	Chemical shift (ppm)	Relative area (%)	Chemical shift (ppm)	Relative area (%)
J	5.32	4.15	5.32	5.25
I	5.22	1.90	5.21	1.42
H	4.24	1.07	4.29	0.43
G	4.16	1.06	4.17	1.82
F	2.77	0.87	2.79	0.64
E	2.23	6.67	2.23	6.32
D	2.02	7.81	2.03	6.96
C	1.61	3.38	1.59	4.26
B	1.30	66.73	1.30	64.64
A	0.89	6.37	0.89	8.26

2.3 PDFF Map Generation

The 6-echo gradient echo CSE data were processed using the MAGO algorithm [3] to produce maps of proton density fat fraction (PDFF) (Fig. 2). This confounder-corrected CSE method uses an input of a multi-peak spectral model for fat. The raw echo data was processed 5 separate times, each time using a different multi-peak spectral model. The spectral models included the two ten-peak breast fat spectra derived above, a nine-peak spectrum derived from subcutaneous adipose tissue [11], a six-peak spectrum derived from subcutaneous adipose tissue [21] and a six-peak spectrum derived from liver fat [12]. Whilst the composition of liver fat and breast adipose tissue are different, the liver fat spectrum is readily available in the clinical setting and well described in literature, therefore it was included in this analysis to enable assessment of its applicability to breast fat in PDFF quantification.

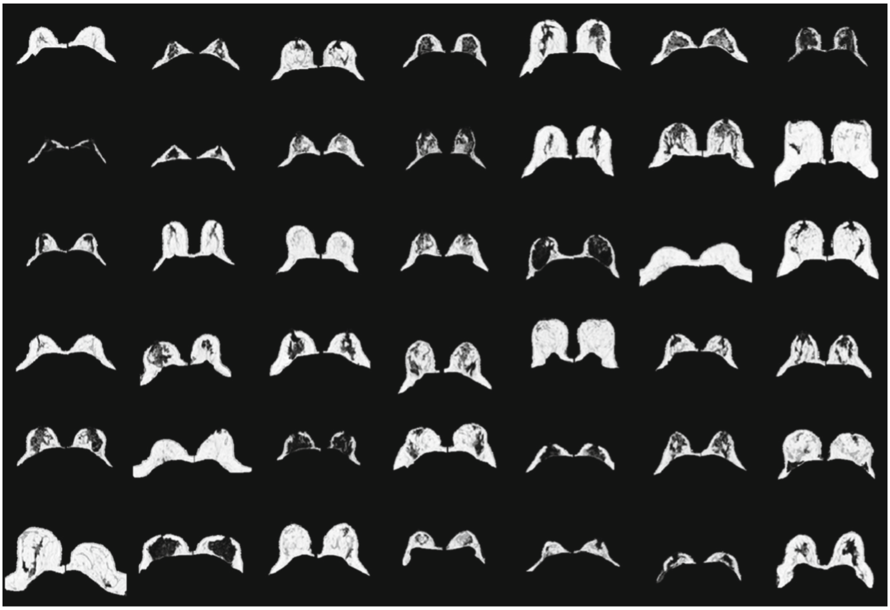

Fig. 2. Examples of central slices of PDFF maps calculated from 3D CSE-MRI.

2.4 Body Masking

A body masking approach was used to separate the breasts from surrounding noise in the PDFF maps. Initial masks were computed in the water and fat images separately by first square-root transforming the image intensities and computing an Otsu threshold. The two masks were morphologically opened using a spherical structuring element with a radius of 3 pixels and then combined into one mask with a logical OR operation. Morphological closing was then applied to the combined mask using the same spherical structuring element to produce the body mask shown in Fig. 3a.

To segment the breasts away from the body outline, the chest wall was manually delineated on the central slice of the proton density fat image. A line was drawn beneath each breast which extended out to the tip of the axillae, as shown in Fig. 3b. A mask was produced to include all pixels above this delineation which was then combined with the body mask calculated in Fig. 3a. This produced a mask of both breasts as shown in Fig. 3b. Figure 3c shows the resulting whole breast segmentation for the 3D CSE acquisition across three different participants.

2.5 Segmentation of Adipose Tissue from Fibrous Tissue

Breast tissue is highly heterogeneous, often containing thin strands of fibrous tissue distributed amongst adipose tissue. To separate fibrous tissue from adipose tissue, the monogenic signal was used as described in Ralli et al. [20] using a log-Gabor filter. Five filters were used with wavelengths 2, 3, 4, 5 and 6 pixels and a σ/f_0 ratio of 0.5 was used. For each CSE acquisition, phase symmetry was computed for the echo image that provided the highest contrast between fibrous and fatty tissue; this was the first echo time in the 3D CSE acquisition and the fourth echo time in the 2D CSE acquisition.

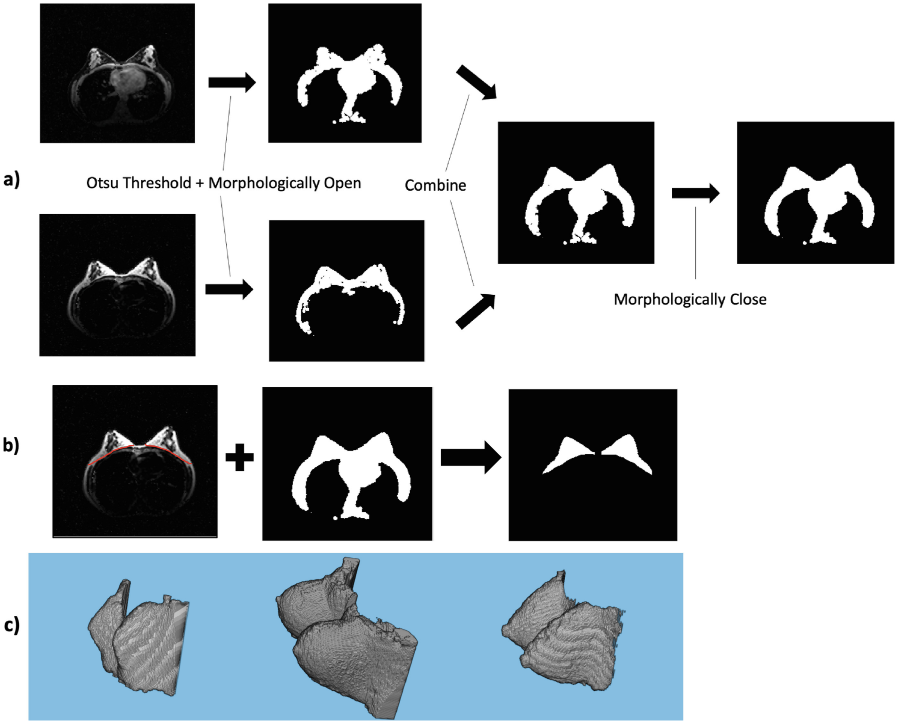

Fig. 3. Overview of segmentation of the whole breast a) Body mask produced from proton density water and fat images using morphology - one example slice shown b) Manual chest delineation combined with body mask to form mask of each breast c) Example whole breast masks produced using 3D CSE acquisitions.

Phase symmetry is computed from the responses of the even (log-Gabor) and odd (Riesz-transformed log-Gabor) filters. Phase symmetry measures the extent to which the even filter response dominates the odd response, and thus quantifies the extent to which a given voxel contains a symmetric feature. It was hypothesised that thin pieces of fibrous tissue surrounded by adipose tissue would have high phase symmetry values. An Otsu threshold was applied to the calculated phase symmetry map to provide a mask which identified thin strands of fibrous tissue.

Whilst the use of phase symmetry maps provided excellent identification of thinner segments of fibrous tissue, larger homogeneous clumps of fibrous tissue in the breast exist, and are especially prevalent amongst younger women. The edges of these areas are readily identified in the phase symmetry maps but the phase symmetry within a homogeneous region of fibrous tissue is approximately equal to the phase symmetry within a homogeneous region of fatty tissue. Therefore a purely phase-symmetry-based approach cannot readily identify these larger areas of fibrous tissue. This is demonstrated in the phase symmetry maps shown in the second column of Fig. 4, where thin strands of fibrous tissue are clearly identified but larger areas of fibrous tissue are not. An additional step ensured larger areas of fibrous tissue were identified and excluded from the masking of breast adipose tissue.

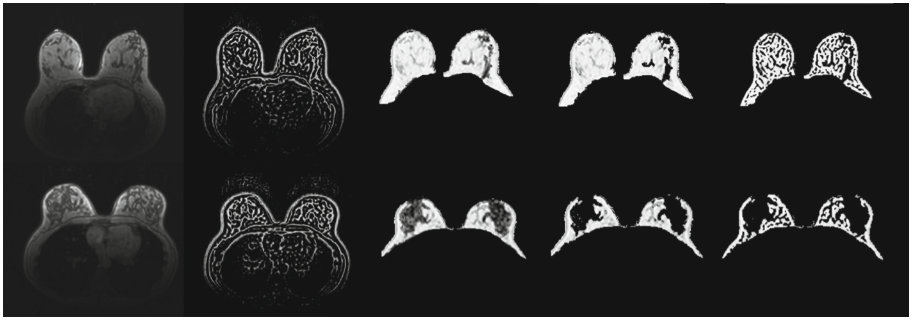

Fig. 4. Overview of adipose tissue segmentation, shown in a single slice of the 3D CSE acquisition for a participant with fatty breasts (top) and a participant with dense breasts (bottom). Left to right: the raw echo image; the phase symmetry map; the PDFF map with the breast mask calculated in Fig. 3b applied; the PDFF map with the threshold determined from multi-modal Gaussian histogram analysis applied; the PDFF map with both the histogram threshold applied and the phase symmetry mask applied.

For each dataset, the whole breast mask (Fig. 3b) was applied to the central slice of the PDFF map calculated using the healthy breast fat spectrum. A histogram was plotted of all PDFF values within this slice. As shown in Fig. 5, a multi-modal Gaussian model with three peaks was fitted to a kernel-smoothed estimate of the histogram using a non-linear least squares approach. The three peaks were hypothesised to correspond to: fibrous tissue (lowest PDFF values), adipose tissue (highest PDFF values) and mixed voxels. A threshold to exclude remaining areas of fibrous tissue was found by calculating the three sigma upper boundary for the central peak as shown in Fig. 5. This was hypothesised to correspond to the PDFF value at which 99.7% of fibrous-tissue-containing voxels were excluded. For each case, the calculation of this threshold value from the histogram distribution was reviewed, and when the multi-modal Gaussian model did not fit well (for example, in very fatty breasts where the two peaks containing fibrous tissue are sparsely populated), a manual threshold was selected through examination of the histogram distributions.

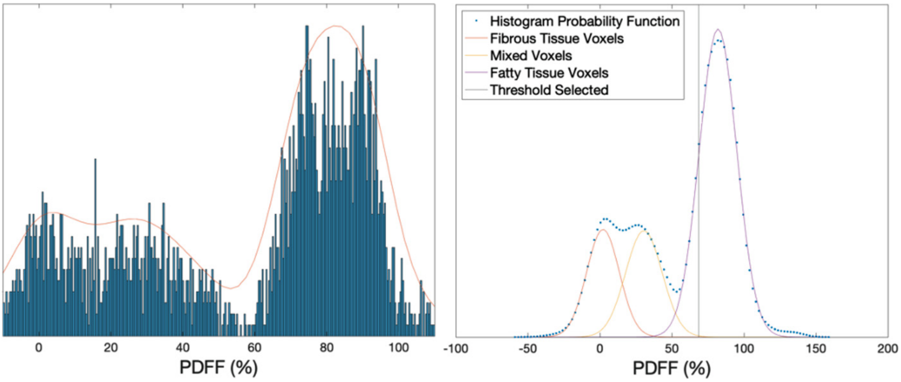

Fig. 5. Left: Example histogram of PDFF values within the central slice of the breast along with the probability density function of the histogram (not to scale). Right: Multi-modal Gaussian fitting to the probability density function of the histogram of PDFF values, showing identification of the threshold value.

To produce the final PDFF maps containing only breast adipose tissue the whole breast mask, the phase symmetry mask and the thresholding value determined from histogram analysis were all applied to the calculated PDFF maps. An overview of this process is shown for two example cases in Fig. 4.

3 Results

3.1 Variation in PDFF with Different Fat Spectra

The variation in PDFF resulting from the use of different fat spectra was measured through examination of the mean PDFF value in the breast adipose tissue of the healthy cohort, using the 3D CSE acquisition for each case. The mean R^2 value for the fit in the breast adipose tissue was also calculated. To obtain a measure of the PDFF of breast fat in each case, the mean PDFF value was calculated within the adipose tissue in the central 40 slices, corresponding to an axial slice stack of 8 cm. This central slice stack was used to exclude the effect of a phase-encoded motion artefact observed in the peripheral slices of the acquisition which contained minimal breast tissue.

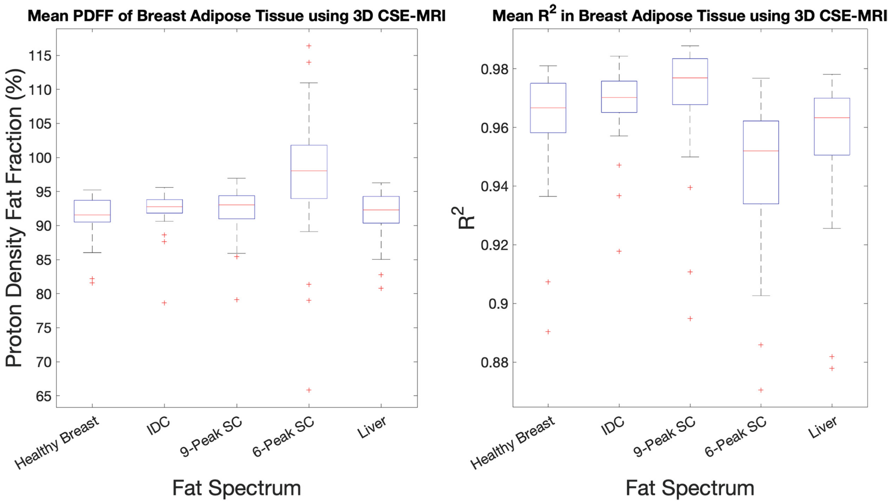

Fig. 6. Left: Box plot displaying variation in mean PDFF of breast adipose tissue as measured with 3D CSE-MRI using different fat spectra. Right: Box plot displaying variation in mean R^2 of PDFF fitting using different fat spectra. Left to right: Healthy breast fat spectrum, breast fat spectrum from participant with IDC, 9-peak subcutaneous fat spectrum, 6-peak subcutaneous fat spectrum, liver fat spectrum.

Figure 6 shows the distribution in measurement of breast adipose tissue PDFF and R^2 values across five different fat spectra. A significant difference was found in PDFF values calculated using the healthy breast fat spectrum and those calculated using the IDC fat spectrum (Wilcoxon rank sum test, $p = 0.028$). Additionally, a significant difference was found in PDFF values calculated using the healthy breast fat spectrum and those calculated using the 9-peak subcutaneous fat spectrum ($p = 0.043$). The 6-peak subcutaneous fat spectrum described by Ren et al. [21] demonstrated a very clear over-estimation of PDFF compared to all four other fat spectra ($p << 0.001$ for all comparisons). The PDFF values produced using the liver fat spectrum were not found to be significantly different to those produced using healthy breast fat ($p = 0.238$).

The overestimation in PDFF calculation of the 6-peak subcutaneous spectrum is reflected in its significantly lower distribution of R^2 values compared to other fat spectra ($p = 0.0029$ compared to liver fat spectrum, $p << 0.001$ for all other comparisons). Utilising the 6-peak liver fat spectrum was found to have significantly poorer R^2 performance than using the healthy breast fat spectra ($p = 0.0456$) or the 9-peak subcutaneous fat spectrum ($p << 0.001$). Though the 9-peak subcutaneous fat spectrum was found to have the highest median R^2, manual review of PDFF images showed that use of this spectrum often resulted in areas of artificially low PDFF due to poor fitting, as shown in Fig. 7. However, as these areas of artificially low PDFF were typically segmented out during the thresholding step described in the Sect. 2.5, such areas of poor fitting are not reflected in Fig. 6.

Fig. 7. Example PDFF map showing region of poor fitting using 9-peak subcutaneous fat spectrum (right) compared to using healthy breast fat spectrum (left).

To demonstrate this, for each case the mask calculated from the PDFF map generated with the healthy breast fat spectrum was applied to all the PDFF maps fitted with different spectra. This mask was manually reviewed against the high resolution T1-weighted acquisition to ensure that it excluded only regions of fibrous tissue and that any areas of adipose tissue which may be poorly fitted would still be included in the mask. As shown in Fig. 8, using the same mask across the different PDFF maps did indeed force these areas of poor fitting to be included. This resulted in the R^2 of PDFF fitting using the 9-peak subcutaneous fat spectrum (median R^2 0.951) being significantly lower than that using the healthy breast fat spectrum (median R^2 0.960, p-value of Wilcoxon rank sum test = 0.0085).

Utilising the healthy breast fat spectra, the median PDFF across breast adipose tissue in a healthy cohort was found to be 91.6 ± 3.0% (IQR 90.5–93.7%).

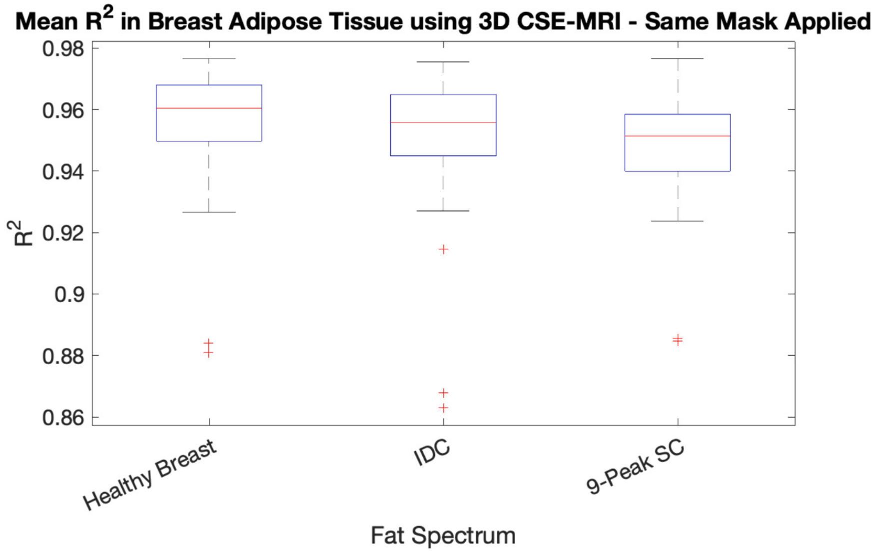

Fig. 8. Box plot displaying variation in mean R^2 of PDFF fitting in breast adipose tissue using the 3D CSE sequence and different fat spectra whilst applying the same adipose tissue mask derived from the use of the healthy breast fat spectrum to all data.

Franz et al. [9] found the PDFF of gluteal fat to be 90.8 ± 4.5% (IQR 81.4–96.2%) when measured with 3D 6-echo CSE-MRI, therefore suggesting similar adipose composition between healthy mammary and gluteal fat.

3.2 Variation in PDFF Calculation Between 2D and 3D CSE Acquisitions

Agreement between the 2D and 3D 6-echo gradient echo CSE acquisitions was assessed through calculation of the 95% Bland-Altman limits of agreement across the nine participants in the healthy cohort who were scanned with both acquisitions (Fig. 9). The mean PDFF value in the central slice was calculated for the 2D and 3D acquisitions, using the healthy volunteer breast fat spectrum. The 95% limits of agreement were −0.72% to 5.54% PDFF, with a bias of 2.41% (2.41 ± 3.13%), suggesting that the 3D acquisition typically measures a higher PDFF value within adipose tissue compared to the 2D acquisition. No trend was observed across the Bland-Altman plot, suggesting that the bias remains reasonably constant across varying PDFF values.

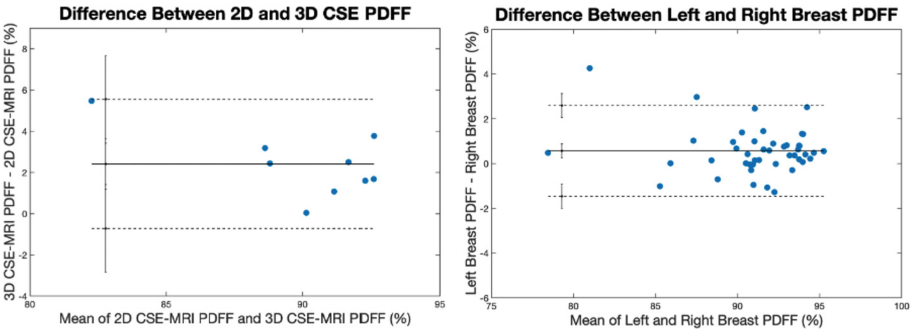

Fig. 9. Bland-Altman plots showing agreement between PDFF values of the breast adipose tissue in a healthy cohort calculated in the central slice of the 2D and 3D CSE acquisitions (left) and agreement between PDFF values of the breast adipose tissue in a healthy cohort calculated in left and right breasts (right). The 95% upper and lower limits of agreement are displayed (dotted lines), along with the confidence intervals for each limit of agreement (solid vertical lines).

3.3 Variation in PDFF Between Left and Right Breast

Agreement in PDFF measurement between left and right breast adipose tissue was assessed in the healthy cohort through calculation of the 95% Bland-Altman limits of agreement (Fig. 9). The mean PDFF value across the central slice stack of the 3D-CSE acquisition described in Sect. 3.1 was calculated for each participant's left breast and right breast, using the healthy volunteer breast fat spectrum. The 95% limits of agreement were −1.46% to 2.60% PDFF with a bias of 0.57% (0.57 ± 2.03%), demonstrating high agreement between the PDFF in breast adipose tissue found in each breast. No trend was observed in left-right breast PDFF agreement across varying PDFF values.

3.4 Variation in PDFF of Perilesional Adipose Tissue

The PDFF of breast adipose tissue immediately surrounding breast lesions was measured through application of user-drawn ROIs to single slices in the 3D CSE acquisition (Fig. 10). This was carried out in one participant with DCIS, one participant with IDC and in two participants with known breast cysts. The mean PDFF values extracted from the ROI in the adipose tissue around each lesion and the mean PDFF of the adipose tissue across the whole slice are displayed in Table 2. Breast cysts which were adjacent to adipose tissue were selected for measurement; note that cyst 2 and cyst 3 were present in the same participant, whilst cyst 1 was taken from a separate participant.

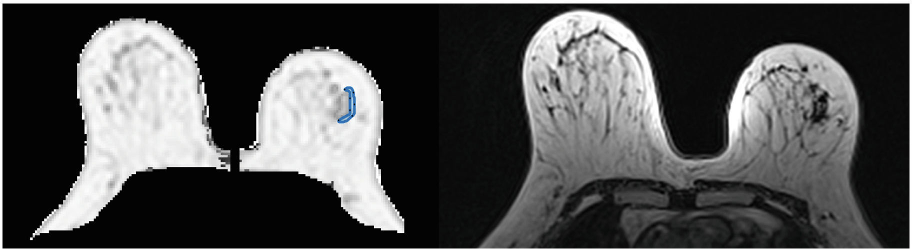

Fig. 10. Example images showing DCIS lesion: PDFF map (left) with user-drawn ROI (shown in blue) in surrounding adipose tissue and high resolution T1-weighted image at most similar slice location (right). (Color figure online)

ROIs were drawn in two adjacent PDFF slices where DCIS was identified and four adjacent slices where IDC was identified. Regions of partial voluming were excluded from the user-drawn ROIs, and inclusion of fibrous tissue was avoided through comparison to the high resolution T1-weighted images acquired at the most similar slice location. The difference in the PDFF of mammary fat around the lesion to the PDFF of mammary fat across the whole slice was found to be larger with DCIS than cysts, with a mean difference of 4.5% PDFF compared to 0.4% PDFF. The difference between the PDFF of perilesional adipose tissue and the PDFF of adipose tissue across the whole slice was found to be largest of all in the participant with IDC, with a mean difference of 5.6%.

Table 2. Table showing mean PDFF of breast adipose tissue surrounding different lesion types alongside the mean PDFF of all breast adipose tissue in the slice containing the lesion. The difference between these values for each lesion is shown, as well as the mean difference for each lesion type.

	DCIS		IDC				Cysts		
	Slice 1	Slice 2	Slice 1	Slice 2	Slice 3	Slice 4	Cyst 1	Cyst 2	Cyst 3
Mean PDFF around lesion (%)	87.5	87.1	86.2	84.3	85.3	83.5	88.6	90.1	91.6
Mean PDFF throughout slice (%)	91.8	91.8	90.3	90.7	90.4	90.3	89.2	89.8	92.5
Difference (%)	4.3	4.7	4.1	6.4	5.1	6.8	0.6	−0.2	0.9
Mean Difference (%)	4.5		5.6				0.4		

4 Discussion

An MR spectrum derived from the adipose tissue of a participant designated as healthy was shown to perform significantly better in breast adipose PDFF calculation than either 6-peak or 9-peak subcutaneous fat spectra. Calculated PDFF values of breast adipose tissue in a healthy cohort suggested a similar composition between breast fat and gluteal fat and the median PDFF across a healthy cohort was found to be 91.6 ± 3.0%; this may have use as a reference value to compare pathology against. Early results indicated that adipose tissue surrounding both invasive and non-invasive cancers demonstrated lowered PDFF values which may be reflective of the browning or inflammation of mammary fat.

Phase symmetry maps enabled identification of thinner strands of fibrous tissue but did not identify larger areas of fibrous tissue such as those often seen in dense breasts. Whilst the use of multi-modal Gaussian fitting of histograms to provide a threshold for the exclusion of larger areas of fibrous tissue was successful, often voxels containing adipose tissue were excluded along with the fibrous tissue. Since the aim of this paper was to examine the PDFF of adipose tissue, exclusion of adipose voxels is preferable to inclusion of voxels containing fibrous tissue. However, for future work where precise identification of areas fibrous tissue may be required, we will explore other methods which do not dispose of spatial information, for example the use of phase asymmetry (rather than phase symmetry) to identify larger areas of homogeneous tissue.

Whilst the 9-peak subcutaneous fat spectrum showed the best R^2 performance when masks were individually calculated for the different PDFF maps, application of the same mask across the PDFF maps demonstrated the increased prevalence of regions of poor fitting when using this subcutaneous fat spectrum. This suggests that an alternative fat spectrum should be used in breast adipose PDFF calculation to ensure accurate quantification throughout the whole breast. When the same mask was applied to all PDFF maps, the R^2 performance was distinctly highest when using the healthy breast fat spectrum.

A significant difference was found amongst a healthy cohort in the PDFF values calculated with a healthy breast fat spectrum and a breast fat spectrum taken from a participant with invasive ductal carcinoma. This finding may prove to be an issue for the use of PDFF as a biomarker of the breast, as it may suggest the need for a fat spectrum particular to the patient's disease state. However, before this conclusion can be made, PDFF calculation with these two spectra would need to be evaluated in a cohort of patients with breast cancer and the effect of spectra from other participants, both those who are healthy and those who have cancer, should be examined. Additionally, the effect of this difference on disease identification with PDFF would need to be assessed; any bias incurred by use of an imperfect spectrum may not effect the sensitivity of PDFF to disease. For example, in Sect. 3.4, the same fat spectrum was used in PDFF calculation across a cohort with varying disease states and a differentiation between benign and malignant lesions was still observed.

The performance of the PDFF fitting was lowest when using the 6-peak liver fat spectrum and the 6-peak subcutaneous fat spectrum which may suggest that identification of more peaks within the fat spectrum leads to improved PDFF fitting within breast adipose tissue. However, the actual PDFF values calculated using the healthy breast fat spectrum were not significantly different from those calculated when using the liver fat spectrum. This suggests potential utility of the liver fat spectrum in measurement of breast adipose PDFF, thereby supporting the IDEAL-IQ maps used in the work of Hisanaga et al. [13].

High agreement and negligible bias were observed between left and right breast adipose PDFF in a healthy cohort, suggesting similar tissue composition. The bias seen in the comparison of 3D CSE PDFF to 2D CSE PDFF could result from the substantially thicker slice used in the 2D CSE acquisition. This may result in the inclusion of small pieces of fibrous tissue within voxels which are identified as containing only adipose tissue, thus lowering the estimate of PDFF compared to that of the 3D CSE acquisition.

Early results from a single invasive ductal carcinoma case agree with the findings of Hisanaga et al. [13] that the fat fraction of breast adipose tissue is distinctly lowered around invasive cancers. Excitingly, perilesional adipose fat fraction was also found to be distinctly lowered around ductal carcinoma in situ, suggesting potential utility of breast adipose PDFF as a biomarker of early-stage, non-invasive cancer.

Whilst these lowered fat fraction values could be caused by the inclusion of voxels with partial voluming artefact in the ROI, the difference between breast adipose PDFF across the whole slice and the PDFF around the lesion was found to be distinctly greater in both cancer cases than in the cases with cysts. This result agrees with the finding that increased browning of mammary fat occurs in proximity to cancerous lesions compared to benign lesions [26]. The lowered fat fraction values in proximity to cancer may also be reflective of inflammation or possibly oedema in the case of the participant with invasive cancer. Data from more participants with cancer, particularly non-invasive subtypes, must be processed and a less variable method of identifying the ROIs around lesions must be found before this result can be reported as significant. An improved method would account for varying amounts of fibrous tissue in proximity to the lesions.

There are several limitations associated with this study. Firstly, the segmentation of whole-breast adipose tissue is currently semi-automatic, requiring user intervention to delineate the chest wall and identify the tips of the axillae. An improved method could use machine learning to identify these anatomical markers, such as that demonstrated by Wei et al. [27]. Secondly, whilst R^2 has proven to be a valuable metric in assessing both the quality of PDFF maps [17] and the performance of different spectral models in PDFF map generation [14], it is not a definitive metric of the accuracy of PDFF calculation. This is not possible without ground truth measurement of fat content, such as that acquired histologically. Computation of other metrics such as the Cramer-Rao lower bound would further aid evaluation of the different spectral models in PDFF calculation. Thirdly, when the same adipose tissue mask was applied to PDFF maps generated with different spectra for the analysis shown in Fig. 8, the mask chosen was that calculated from the PDFF map processed with the healthy breast fat spectrum. This mask was chosen as it was manually reviewed to accurately include breast adipose tissue and not to exclude any regions of artificially lowered PDFF, such as those shown in Fig. 7. To avoid bias which may be incurred by applying an adipose tissue mask calculated using a particular fat spectrum, an improved method would apply a mask calculated from a separate MR sequence and co-register back to the CSE-MRI sequence. Finally, biopsy-induced effects such as oedema may affect the PDFF of adipose tissue adjacent to lesions. The biopsy for both participants with confirmed cancer was completed at least 4 weeks prior to their MRI scan, compliant with the guidelines in Ko et al. [15], though future work should include assessment of fat adjacent to needle-naive tumours.

To our knowledge, this work is the first to implement a breast-specific fat spectrum into the calculation of breast adipose PDFF and the first to have reported this parameter in a healthy cohort. We believe that with additional work across a more varied patient cohort, this parameter has exciting potential to characterise the breast parenchyma and identify early-stage cancer growth.

References

1. Breast cancer incidence (invasive) statistics, July 2021. https://www.cancerresearchuk.org/health-professional/cancer-statistics/statistics-by-cancer-type/breast-cancer/incidence-invasive
2. Almekinders, M.M., et al.: Breast adipocyte size associates with ipsilateral invasive breast cancer risk after ductal carcinoma in situ. npj Breast Cancer **7** (2021). https://doi.org/10.1038/s41523-021-00232-w
3. Bagur, A.T., Hutton, C., Irving, B., Gyngell, M.L., Robson, M.D., Brady, M.: Magnitude-intrinsic water-fat ambiguity can be resolved with multipeak fat modeling and a multipoint search method. Magn. Reson. Med. **82**, 460–475 (2019). https://doi.org/10.1002/mrm.27728
4. Bancroft, L.C.H., et al.: Proton density water fraction as a reproducible MR-based measurement of breast density. Magn. Reson. Med. (2021). https://doi.org/10.1002/mrm.29076, https://onlinelibrary.wiley.com/doi/10.1002/mrm.29076

5. Bos, S.A., Gill, C.M., Martinez-Salazar, E.L., Torriani, M., Bredella, M.A.: Preliminary investigation of brown adipose tissue assessed by PET/CT and cancer activity. Skeletal Radiol. **48**, 413–419 (2019). https://doi.org/10.1007/S00256-018-3046-X, https://link.springer.com/article/10.1007/s00256-018-3046-x
6. Boyd, N.F., Martin, L.J., Yaffe, M.J., Minkin, S.: Mammographic density and breast cancer risk: current understanding and future prospects. Breast Cancer Res. BCR **13** (2011). https://doi.org/10.1186/BCR2942, https://pubmed.ncbi.nlm.nih.gov/22114898/
7. Cao, Q., et al.: A pilot study of FDG PET/CT detects a link between brown adipose tissue and breast cancer. BMC Cancer **14**, 126 (2014). https://doi.org/10.1186/1471-2407-14-126, https://www.ncbi.nlm.nih.gov/pmc/articles/PMC3937456/
8. Caussy, C., Reeder, S.B., Sirlin, C.B., Loomba, R.: Non-invasive, quantitative assessment of liver fat by MRI-PDFF as an endpoint in NASH trials. Hepatology (Baltimore, Md.) **68**, 763 (2018). https://doi.org/10.1002/HEP.29797, https://www.ncbi.nlm.nih.gov/pmc/articles/PMC6054824/
9. Franz, D., et al.: Differentiating supraclavicular from gluteal adipose tissue based on simultaneous PDFF and T2* mapping using a 20-echo gradient-echo acquisition. J. Magn. Resonan. Imaging **50**, 424 (2019). https://doi.org/10.1002/JMRI.26661, https://www.ncbi.nlm.nih.gov/pmc/articles/PMC6767392/
10. Freed, M., et al.: Evaluation of breast lipid composition in patients with benign tissue and cancer by using multiple gradient-echo MR imaging. Radiology **281**, 43–53 (2016). https://doi.org/10.1148/radiol.2016151959
11. Hamilton, G., et al.: In vivo triglyceride composition of abdominal adipose tissue measured by 1H MRS at 3T. J. Magn. Resonan. Imaging **45**, 1455–1463 (2017). https://doi.org/10.1002/jmri.25453
12. Hamilton, G., et al.: In vivo characterization of the liver fat ^{1}H MR spectrum. NMR Biomed. **24**, 784–790 (2011). https://doi.org/10.1002/NBM.1622, https://pubmed.ncbi.nlm.nih.gov/21834002/
13. Hisanaga, S., et al.: Peritumoral fat content correlates with histological prognostic factors in breast carcinoma: a study using iterative decomposition of water and fat with echo asymmetry and least-squares estimation (IDEAL). Magn. Reson. Med. Sci. **20**, 28–33 (2021). https://doi.org/10.2463/mrms.mp.2019-0201
14. Hong, C.W., et al.: MRI proton density fat fraction is robust across the biologically plausible range of triglyceride spectra in adults with nonalcoholic steatohepatitis. J. Magn. Reson. Imaging **47**, 995–1002 (2018). https://doi.org/10.1002/jmri.25845
15. Ko, Y.H., Song, P.H., Moon, K.H., Jung, H.C., Cheon, J., Sung, D.J.: The optimal timing of post-prostate biopsy magnetic resonance imaging to guide nerve-sparing surgery. Asian J. Androl. **16**, 280–284 (2014). https://doi.org/10.4103/1008-682X.122190
16. Kolb, T.M., Lichy, J., Newhouse, J.H.: Comparison of the performance of screening mammography, physical examination, and breast us and evaluation of factors that influence them: an analysis of 27,825 patient evaluations. Radiology **225**, 165–175 (2002). https://doi.org/10.1148/RADIOL.2251011667, https://pubmed.ncbi.nlm.nih.gov/12355001/
17. Middleton, M., et al.: A quantitative imaging biomarker assessment metric for MRI-estimated proton density fat fraction. Hepatology, AASLD Abstracts **66**, 1113–1114 (2017)
18. Nieman, K.M., et al.: Adipocytes promote ovarian cancer metastasis and provide energy for rapid tumor growth. Nat. Med. **17**, 1498–1503 (2011). https://doi.org/10.1038/nm.2492

19. Panzironi, G., Moffa, G., Galati, F., Marzocca, F., Rizzo, V., Pediconi, F.: Peritumoral edema as a biomarker of the aggressiveness of breast cancer: results of a retrospective study on a 3 T scanner. Breast Cancer Res. Treat. **181**(1), 53–60 (2020). https://doi.org/10.1007/s10549-020-05592-8
20. Ralli, G.P., Ridgway, G.R., Brady, S.M.: Segmentation of the biliary tree from MRCP images via the monogenic signal. Commun. Comput. Inf. Sci. 1248 CCIS, 105–117 (2020). https://doi.org/10.1007/978-3-030-52791-4_9. https://link.springer.com/chapter/10.1007/978-3-030-52791-4_9
21. Ren, J., Dimitrov, I., Sherry, A.D., Malloy, C.R.: Composition of adipose tissue and marrow fat in humans by 1H NMR at 7 Tesla. J. Lipid Res. **49**, 2055–2062 (2008). https://doi.org/10.1194/jlr.D800010-JLR200
22. Rodge, G.A., Goenka, M.K., Goenka, U., Afzalpurkar, S., Shah, B.B.: Quantification of liver fat by MRI-PDFF imaging in patients with suspected non-alcoholic fatty liver disease and its correlation with metabolic syndrome, liver function test and ultrasonography. J. Clin. Exp. Hepatol. **11**, 586–591 (2021). https://doi.org/10.1016/J.JCEH.2020.11.004
23. Sun, S., et al.: Exosomes from the tumour-adipocyte interplay stimulate beige/brown differentiation and reprogram metabolism in stromal adipocytes to promote tumour progression. J. Exp. Clin. Cancer Res. CR **38** (2019). https://doi.org/10.1186/S13046-019-1210-3, https://pubmed.ncbi.nlm.nih.gov/31138258/
24. Torre, L.A., Islami, F., Siegel, R.L., Ward, E.M., Jemal, A.: Global cancer in women: burden and trends. Cancer Epidemiol. Biomarkers Prevention : a publication of the American Association for Cancer Research, cosponsored by the American Society of Preventive Oncology **26**, 444–457 (2017). https://doi.org/10.1158/1055-9965.EPI-16-0858, https://pubmed.ncbi.nlm.nih.gov/28223433/
25. Vaysse, C., et al.: Inflammation of mammary adipose tissue occurs in overweight and obese patients exhibiting early-stage breast cancer. npj Breast Cancer **3** (2017). https://doi.org/10.1038/s41523-017-0015-9
26. Wang, F., et al.: Mammary fat of breast cancer: gene expression profiling and functional characterization. PloS One **9** (2014). https://doi.org/10.1371/JOURNAL.PONE.0109742, https://pubmed.ncbi.nlm.nih.gov/25291184/
27. Wei, D., Weinstein, S., Hsieh, M.K., Pantalone, L., Kontos, D.: Three-dimensional whole breast segmentation in sagittal and axial breast MRI with dense depth field modeling and localized self-adaptation for chest-wall line detection. IEEE Trans. Biomed. Eng. **66**, 1567–1579 (2019). https://doi.org/10.1109/TBME.2018.2875955
28. Zhu, Z.R., et al.: Fatty acid composition of breast adipose tissue in breast cancer patients and in patients with benign breast disease. Nutrition Cancer **24**, 151–160 (1995). https://doi.org/10.1080/01635589509514403, https://pubmed.ncbi.nlm.nih.gov/8584451/